Surface & Coatings Technology 302 (2016) 368–382

Contents lists available at ScienceDirect

Surface & Coatings Technology

journal homepage: www.elsevier.com/locate/surfcoat

Effects of angular injection, and effervescent atomization on high-velocity suspension flame spray process

Mahrukh Mahrukh [a,b], Arvind Kumar [c], Sai Gu [d,*]

[a] School of Energy, Environment and Agrifood, Cranfield University, Cranfield, Bedfordshire MK43 0AL, UK
[b] Department of Mechanical Engineering, NED University of Engineering & Technology, University Road, 75270 Karachi, Pakistan
[c] Department of Mechanical Engineering, Indian Institute of Technology Kanpur, Kanpur 208016, Uttar Pradesh, India
[d] Department of Chemical and Process Engineering, Faculty of Engineering and Physical Sciences, University of Surrey, GU2 7XH, UK

ARTICLE INFO

Article history:
Received 25 February 2016
Revised 9 June 2016
Accepted in revised form 10 June 2016
Available online 11 June 2016

Keywords:
Nanoparticle
Suspension
HVSFS process
Effervescent atomization
Angular injection

ABSTRACT

This work presents the nanostructured coating formation using suspension thermal spraying through the HVOF torch. The nanostructured coating formation requires nanosize powder particles to be injected inside a thermal spray torch using liquid feedstock. The liquid feedstock needs to be atomized when injected into the high-velocity oxygen fuel (HVOF) torch. This paper presents the effects of angular injection and effervescent atomization of the liquid feedstock on gas and droplet dynamics, vaporization rate, and secondary breakup in the high-velocity suspension flame spray (HVSFS) process. Different angular injections are tested to obtain the optimum value of the angle of injection. Moreover, effervescent atomization technique based on twin-fluid injection has been studied to increase the efficiency of the HVSFS process. Different solid nanoparticle concentrations in suspension droplets are considered. In angular injection the droplets are injected into the core of the combustion zone; this immediately evaporates the droplets, and evaporation is completed within the torch. The value of 10°–15° is selected as the optimal angle of injection to improve the gas and droplet dynamics inside the torch, and to avoid the collision with the torch's wall. The efficiency of the effervescent atomization can be enhanced by using high gas-to-liquid mass flow rate ratio, to increase the spray cone angle for injecting the suspension liquid directly into the combustion flame. It is also found that the increment in the nanoparticle concentration has no considerable effects on the droplet disintegration process. However, the location of evaporation is significantly different for homogeneous and non-homogeneous droplets.

1. Introduction

The thermal spraying technology for producing thermal barrier and wear-resistant dense coatings can be modified with nanosize powder injection to obtain lower coating thickness. In the frame of thermal spraying techniques, a liquid feedstock system has been developed for injecting nanometre size to 10 μm size powder particles in thermal spraying torch [1–3]. The suspension spraying works well for several applications including thermal barrier coatings (TBC), tribofunctional and wear-resistant coatings, biofunctional coatings, fuel cell development, and creating coatings for catalytically active surfaces [3–6]. The HVOF based suspension spraying, named as high-velocity suspension flame spraying (HVSFS) process, uses nanosize powder in the form of liquid suspension [2]. The high-velocity oxygen fuel (HVOF) torches are modified, and the liquid feedstock is injected with the aid of suspension feeder and suspension injector [3,7,8].The HVOF applications use axial (internal) injections [6–10]. This suspension liquid is injected into the flame spray jet and under the action of the combustion gas thermal energy and high-velocity the suspension droplets disintegrate, evaporate and release the nanoparticles inside the torch. These nanoparticles/nano-agglomerates become heated, melted and accelerated towards a prepared surface, and produce a coating on it. The advantage is that the precursor can be nanosize, and the coatings can be thin, smooth and finely structured, even nanostructured [10]. This is not possible with standard dry powder feeders.

In the HVSFS process, the size of microstructural features within the coatings is governed by the liquid feedstock [11–13]. In studies reported in [14], the HVSFS process based on nanosize powder suspension resulted in small and well-flattened lamellae (thickness range 100 nm to 1 μm). The coating exhibited low porosity as compared to Air Plasma Spraying (APS) and HVOF coating and showed better sliding wear resistance [14]. In suspension spraying processes the size of nanostructured coatings depend on a number of parameters, including flame temperature and velocity, suspension feed rate, suspension concentration, suspension's solvent properties, and the atomization of liquid feedstock streams. It was further revealed that the nanoparticles agglomerates size and nanostructured coatings morphology are significantly

* Corresponding author.
E-mail address: sai.gu@surrey.ac.uk (S. Gu).

http://dx.doi.org/10.1016/j.surfcoat.2016.06.028

dependent on the suspension's concentration, viscosity, and surface tension [8,15–21].

The HVOF process efficiency mainly depends on the type of torch, the coating material, the nanoparticles injection parameters, the type of liquid used for suspension preparation, and the distance between the torch and substrate. For increasing the effectiveness of this process, optimization of these parameters is essential. The flow physics inside the HVOF torch is difficult to be studied experimentally, and hence, Computational Fluid Dynamics (CFD) techniques are widely used to understand this. Various models are implemented to understand the complex flow physics, combustion chemistry, flames, and jets formation, and propagation involved in the thermal spraying processes [22–27]. Li and Christofides [22,28–31] highlighted the multi-scale behaviour of the overall process inside a HVOF thermal spray torch (Diamond Jet hybrid gun). They divide the process dynamics into two main parts, first is gas dynamics, and the other is particle dynamics (or in-flight particle behaviour). Both parts highly depend on specific parameters. Gas dynamics have a varied temperature, pressure, velocity, etc. depending on the type of fuel and fuel/oxygen ratio used for combustion. Particle dynamics is dependent on the injection mass flow rate, particle size and shape, injection velocity, the angle of spray and spray distance, etc. Moreover, the fuel/oxygen ratio plays a very important role in particle heating. State-of-the-art CFD techniques are required to make the actual process more effective by developing the role of these parameters and their optimization.

Dongmo et al. [12] performed the first numerical modelling of angular injection in the HVSFS torch. Both liquid ethanol droplets (300 μm) and solid Titania particles (0.5–50 μm) are injected as discrete phases. The evaporation of ethanol droplets shows significant cooling of the combustion gases at a 0° angle of injection. Hence, the authors modified the injection phenomena by simulating the flow with an angle of injection of 30°. They found that injection at an angle of 30° improves the rate of ethanol evaporation inside the combustion chamber (CC) and cooling is reduced. The disadvantage of angular injection is the impingement of droplets and particles to the CC walls and increase in the residence time of particles. Dongmo et al. [13] further analysed an optimized HVSFS torch, where the TopGun-G's is modified by designing a conical shape CC. It increases the process efficiency and helps to avoid nanoparticles contact with the CC walls. In these studies, the authors ignored the effect of nanoparticles loading on properties of pure ethanol, its evaporation process in the HVOF torch and on gas combustion dynamics.

Moreover, to improve the process efficiency of generating the dense nanosized coating, the atomization of droplets is essentially required for suspension carrying high concentrations of suspended particles. The atomization of liquid feedstock can be controlled by the atomizer nozzle design and its injection parameters [32–34]. Many researchers have studied the phenomenon of atomization and some specific work is highlighted here. The theory explained by Castleman in 1930 [35], states that atomization is due to the aerodynamic interaction between the liquid and gas leading to an unstable wave growth on the liquid jet surface. The fast moving air strikes the water jet. Hence, the portion of the liquid mass is drawn out into fine ligaments and turns into small droplets. The higher the air speed, the smaller the size of ligaments/droplets [35]. The atomization of liquid jet is a step-wise process [36]. The near field jet breakup process is dominated by the shedding of liquid sheets and ligaments. The far field has a secondary breakup phenomenon in which the disintegrated liquid lumps from the jet are fragmented by the high-velocity air jets.

The disintegration of liquid feedstock droplets can increase the efficiency of the thermal spraying process, and it is achieved by using an atomizer or a mechanical injector [37–39]. Depending on the availability and application requirements, different atomization gases and processes can be used for atomizing the liquid streams. One method is to introduce atomization-gas by a gas envelope around the liquid jet injection [38]. The high-velocity oxygen gas exerted a force on the liquid jet and atomized the stream into fine droplets. The nanoparticles coating obtained after this type of atomization had a narrow particle size distribution, ranging from 10 to 20 nm [38]. For solution precursor atomization, nitrogen gas was used for the formation of ceramic [39]. The nitrogen flow tube was aligned with the axis of the flame nozzle, and the liquid was fed through the second capillary tube at right angles. The nitrogen flow atomizes the precursor stream at the tip of the liquid-carrying capillary. The syringe pump was used for liquid injection with a flow rate of 50 μl/s and atomizing nitrogen gas flow rates are set to 0.028 l/s. By using this atomization technique, characterization of the spray was performed by the phase-Doppler particle analyzer system that acquired 20,000 simultaneous droplet size and velocity measurements. The droplet size distribution observed from phase-Doppler particle analyzer was in the range of 1–20 μm with a number averaged diameter of about 10 μm. The droplet velocities were in the range of 5–30 m/s, while the number averaged droplet velocity was measured to be 16 m/s. The average splat size was about 30–35 μm, which was generated from droplet sizes of 1–20 μm upon impact [39].

Furthermore, another type of atomization method is effervescent atomization. This technique is twin-fluid atomization, in which a small amount of gas is injected into the liquid before the exit orifice to form a bubbly mixture of gas and liquid. On emerging from the nozzle, due to the pressure difference, gas bubbles rapidly expand and shatter the liquid into ligaments and fine droplets. This method offers the advantage of smaller drop sizes at low injection pressure and atomizing even high viscosity liquids effectively [32–34,40–44]. The droplets size and distribution are dependent on the suspension concentration, viscosity, and surface tension which was extensively analysed by the researchers [33,43,45,46].

Researchers also presented the numerical modelling of effervescent atomization's internal and external flow regimes [33,41,43,44,46]. Esfarjani and Dolatabadi studied the droplets disintegration and two-phase flow structure inside the effervescent atomizer [47] using a broad range of nanoparticles types and concentrations for suspension plasma spray process where no effect on the performance of effervescent atomizer was observed [47]. Furthermore, to capture the external two-phase flow of an effervescent atomizer, a three-dimensional model based on the Navier-Stokes equation is developed by Qian et al. [33]. They analysed the effect of varied injection parameters on the Sauter Mean Diameter (SMD). Based on extensive computations, a fitting formula, by using curve fitting techniques, is obtained that relates the droplet SMD to the operating conditions including injection pressure, gas-to-liquid mass flow rate ratio (GLR), injector exit diameter, and liquid physical properties including viscosity and surface tension [33]. Their results showed that liquid viscosity has a small effect on droplet size and its distribution, and the effervescent atomizer can work efficiently even with highly viscous fluids.

Moreover, they also suggested that smaller liquid density and surface tension will give finer droplet atomization, and the atomization phenomena can easily be studied by droplet Weber ($We = \frac{\rho_d v_{rel}^2 d}{\sigma}$) and Ohnesorge number ($Oh = \frac{\mu}{\sqrt{\rho_d \sigma d}}$) [46]. They also simulated the effect of atomizer operating conditions on particle characteristics in suspension plasma spraying (SPS). Their model predicted the nanoparticles size, trajectory, velocity, and temperature during the Radio Frequency SPS [48]. The disintegration of droplets is influenced by variation in GLR, atomizer orifice exit diameter and injection pressures. Smaller values of GLR would decrease the atomization while the larger orifice diameter would result in larger liquid droplets, and the smaller value of the injection pressure could also affect the atomization process adversely. Hence, for increasing the efficiency of effervescent atomization higher values of GLR and injection pressure with smaller orifice exit diameter should be used [33,43,48].

Furthermore, Fung et al. [49] experimentally and numerically studied the spray atomization under low pressures. The primary atomization Linear Instability Sheet Atomization (LISA) model available in

Fluent was employed to capture the atomized flow from a nasal spray device; while Taylor Analogy Breakup (TAB) model was used to capture the secondary breakup of droplets. Moreover, the experiments were performed to characterize the external flow using a high-speed camera imaging and particle/droplet image analysis. They concluded that controlling the liquid sheet constant and spread parameter in the LISA model would predict the spray cone shape and droplet size distribution for low-pressure applications (0.3–0.5 MPa injection pressure).

In the light of the above-reviewed literature, it is found that no research has been conducted to examine the effect of increasing nanoparticle concentrations on the gas flow dynamics and the droplet dynamics inside the HVSFS torch. All these existing studies ignored the impact of nanoparticles loading on the alteration of properties of pure ethanol, and its disintegration and evaporation processes in the HVOF torch. Moreover, the effect of increasing the nanoparticles loading on the combustion gas dynamics was also not considered. Furthermore, the effects of varying injection parameters and injection types over the flow process physics inside the spray torch have not been studied previously. It must be noted that this analysis needs to be implemented to inspect the effectiveness of the various injection processes. These shortcomings are addressed in this work. In the present work, for atomizing the suspension liquid into fine droplets inside the CC of the HVOF torch, a new effervescent atomizer is designed based on previous research studies [33,34,44]. A numerical model is used to study the effect of varying injection types on the HVOF flow dynamics. For understanding the atomization of the suspension droplet, results are presented and compared for three types of injections, namely surface-type injection (STI), group-type injection (GTI) and effervescent-type injection (ETI).

2. Model description

The HVOF gun geometry used in this study is Diamond Jet DJ2700-torch (Sulzer Metco, Wohlen, Switzerland) [50,51]. The operating parameters, along with the schematic representation of the computational domain, are shown in Fig. 1 and Table 1. The total inlet radius of the CC is $R_{CC} = 9.1$ mm, with length $L_{CC} = 23.8$ mm (named as section-I). The radius at nozzle throat is $R_T = 4.2$ mm, with the extended diverging section acting as the barrel of the gun with length $L_B = 66.2$ mm (section-II) and exit radius $R_B = 6.215$ mm. The free jet domain length (L_{FJ}) is set to 200 mm (section-III) to see the flow dynamics in the far field region after the gun's outlet. The torch geometry considered in the numerical simulations is axisymmetric. The premixed oxygen/fuel (O/F) is injected into the DJ2700 gun; the resulting hot combustion gases are accelerated inside the convergent-divergent (C-D) nozzle and flow through the barrel section towards the exit of the gun. The droplets' injection mass flow rate and injection velocity are selected on the basis of previous work [50–53] (Table 1).

Table 1
Geometric parameters and working conditions for HVSFS thermal spray torch.

Geometric parameters	Symbols	Dimensions (mm)
(I) Combustion chamber length	L_{CC}	23.8
Combustion chamber radius	R_{CC}	9.10
Nozzle throat radius	R_T	4.20
(II) Barrel length	L_B	66.2
Barrel exit radius	R_B	6.22
(III) Free jet length	L_{FJ}	200
Working conditions		
Oxygen flow rate	0.014 kg/s	Initial temperature, 300 K
Air flow rate	0.002 kg/s	
Fuel flow rate	0.004 kg/s	
Droplet constant diameter	150 μm	
Droplet flow rate and initial velocity	0.0001 kg/s, 42 m/s	

The gas dynamics of the HVSFS process is a compressible reacting flow, featuring turbulence and subsonic/sonic/supersonic transitions. The computation of the gas dynamics together with the droplet dynamics provides detailed information for the gas flow field which is required to predict the overall flow dynamics [54]. Firstly, the model simulates the temperature and velocity fields of the HVSFS flame jet for an industrial DJ2700 torch. The Realizable $k-\varepsilon$ model is used for modelling the turbulence in the jet, including the compressibility effects [55,56]. The thermal and flow fields of the combustion gas are solved by the Eulerian approach and the eddy dissipation model (EDM) is employed to model premixed (oxygen/propane) combustion with the hyper-stoichiometric oxygen mass fraction [57–59].

After complete simulation of the gas phase, ethanol droplets carrying suspended nanoparticles are injected into the HVSFS flame jet where they experience several stages. The first stage is the aerodynamic breakup of droplets, as the slow moving droplets are entrained into the jet and accelerate in the high-velocity gas stream. Based on size and thermophysical properties of the liquid and their interaction with the surrounding gas, droplets undergo severe deformation and then breakup into smaller droplets [50–53]. Here, different injection types are studied, namely surface-type injection (STI), group-type injection (GTI) and effervescent-type injection (ETI). The injector exit diameter is $D_{inj} = 1.2$ mm for STI, GTI and ETI cases (see Fig. 2a, b, and c). The first type of injection is analysed for axial droplet injection into the torch from a centralized inlet opening. In the STI, the angle of injection is $\alpha = 0°$, and the suspension droplets move along the centreline axis of the torch (Fig. 2a). Whereas, during angular injection, the GTI method

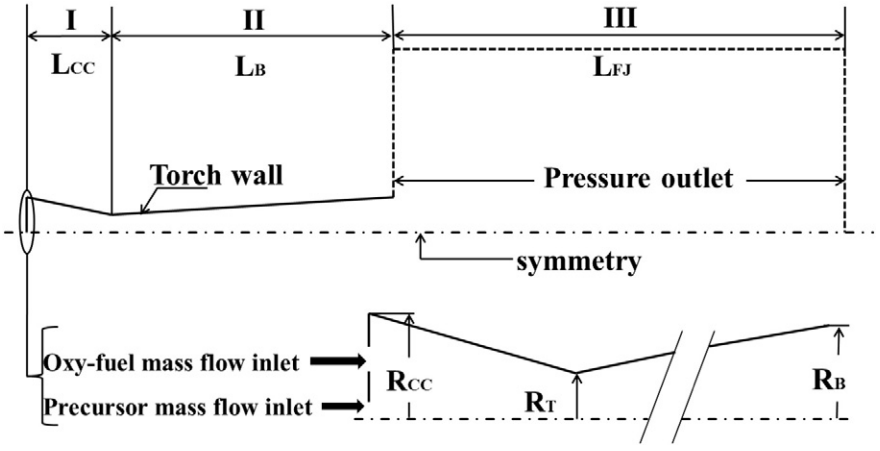

Fig. 1. Schematic of DJ2700 torch showing axisymmetric computational domain with boundary conditions [the domain sections marked as (I) combustion chamber (CC), (II) barrel and (III) free jet regions].

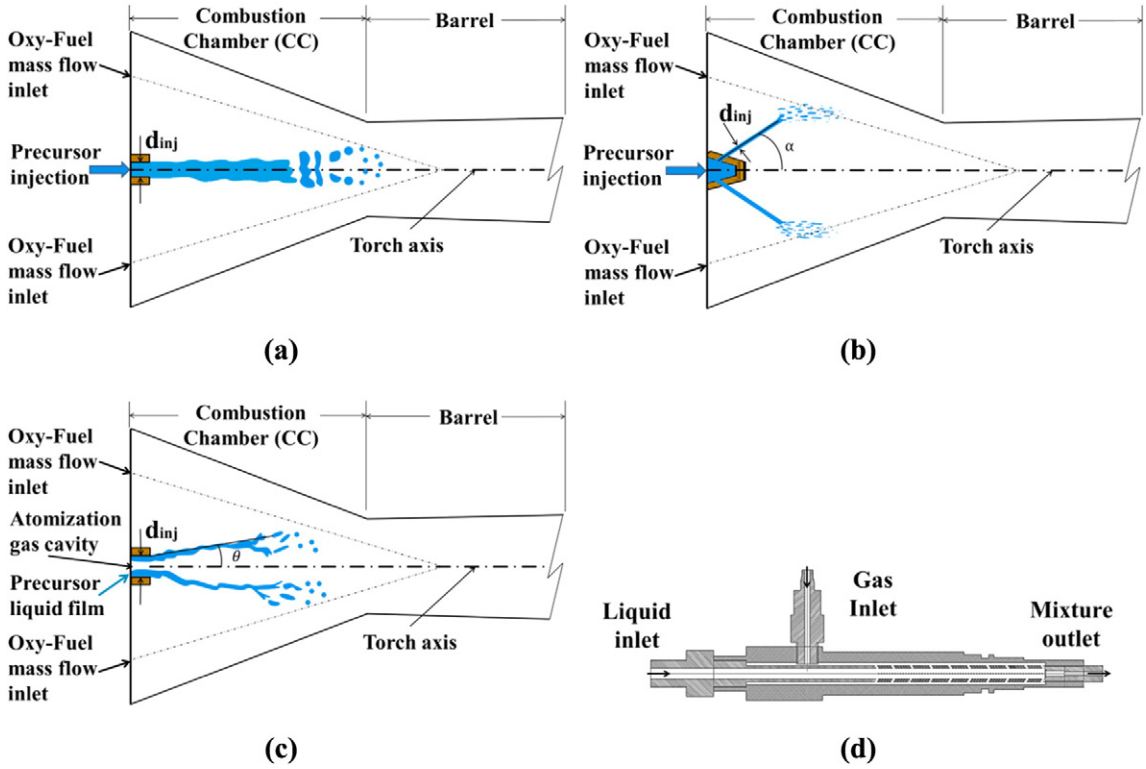

Fig. 2. Schematic of liquid feedstock injection inside the DJ2700 torch (a) surface-type injection (STI) (b) group-type injection (GTI) (c) effervescent-type injection (ETI), and (d) design of effervescent-type injection-nozzle.

is used, in which the streams of droplets are released at varying angles of injection of $\alpha = 5°$, 10°, 15°, and 20° with respect to the axial direction from each facet of the injection surface (Table 2). In GTI, the droplets are injected into the core of the combustion zone and reach the evaporation point rapidly in comparison to the STI and evaporate completely within the torch (Fig. 2b).

The third type of injection uses the twin-fluid phenomenon in which nitrogen gas and liquid feedstock are injected separately into the effervescent-type nozzle. This creates a bubbly flow inside the injection nozzle and then sprays it into the torch's CC to obtain a finer disintegration of the suspension's droplets (Fig. 2c and d). With this technique, the liquid discharged from the orifice with the internal cavity of gas, as shown in Fig. 2c. The motion of the liquid at the exit of the injector creates a gas-core surrounded by the liquid film, and due to the pressure difference gases expand and shatter the liquid film into ligaments and fine droplets [32–34,40,42–44]. For the ETI, different spray-half-angles of $\theta = 4°$, 6°, and 8° are selected based on various GLRs of 0.095, 0.190 and 0.285, respectively (Table 2). It should be noted that increasing the GLR will eventually increase the spray-half-angle which can further improve the atomization.

For the numerical simulations, the history of suspension droplets is computed with Lagrangian formulation where the finite interphase transport rates and the effects of turbulence interactions between the droplet and gas phases are considered [9,12,13,51]. By using this treatment, the evaporation history and temperature change for droplets can be calculated during the second process of heat exchange between the gaseous and liquid phases. The EDM is also used to model non-premixed combustion of ethanol vapours with remnant oxygen left from premixed (oxygen/propane) combustion [57–59]. The heat and mass transfer of the droplets with the continuous phase is modelled using three laws, as described in the previous work [50–53,60]. Detailed descriptions of the gas phase, discrete phase, breakup and combustion models are reported elsewhere [25,27,30,51,54,59,61–63]. The employed mathematical models have been strongly tested against experimental and numerical data [50,52–54,60,64,65], the test results are not repeated here for brevity. Only the detailed modelling equations for the ETI are presented here for a clear understanding in Section 2.1 [33,49].

The suspension properties (viz., surface tension, viscosity, density, specific heat and thermal conductivity) are calculated from commonly

Table 2
Case description with injection types and injection parameters for HVSFS process.

Injection types
Case 1 → Without Droplets, only combustion gas flow characteristics
Case 2.1 → Surface-type injection, angle of injection 0°

Group-type injection		Effervescent-type injection		
Cases	Angle of injection (α)	Cases	Spray-half-angle (θ)	GLR
Case 2.2	5°	Case 3.1	4°	0.095
Case 2.3	10°	Case 3.2	6°	0.190
Case 2.4	15°	Case 3.3	8°	0.285
Case 2.5	20°			

used nanofluids theoretical models [66–68]. Moreover, the temperature dependent pure liquid properties are incorporated, and curve-fitting procedures are applied in the required temperature range as in previous work [52,53,69] and not repeated here for conciseness. For each type of droplet injection (axial, angular and effervescent), different rates of evaporation and fragmentation have been detected. Also, the effect of droplets breakup and evaporation on gas dynamics is changed with varying injection parameters (Table 2). It is due to the variations in droplet interaction with the continuous combustion gases inside the HVSFS torch (see details in results Section 3).

2.1. Droplet injection properties and model equations

Numerous cases are simulated to analyse the effects of varying injection schemes on the droplet atomization in the CC of the thermal spray gun. A clear case representation can be seen in Table 2. Here, Without Droplets (Case 1) refers to a case in which droplets are not injected, and only combustion gas flow characteristics in the HVSFS process are analysed. For the STI scheme (Case 2.1) the suspension droplets are injected axially along the torch axis (with an angle of 0°). In the GTI, different angles of injection at $\alpha = 5°, 10°, 15°$, and 20° are considered for suspension injection and cases are named as Cases 2.2, 2.3, 2.4, and 2.5, respectively (Table 2). Firstly, the effects of angular injection over the torch's flow dynamics are studied with constant droplet diameters of 150 μm at the nanoparticle concentration of 0, 5, 15, and 25 wt.%. Then a similar study is repeated for ETI with the assumption of different spray-half-angles of $\theta = 4°$, 6° and 8° based on varying GLR and those studies are named as Cases 3.1, 3.2 and 3.3, respectively (see Table 2). Different values of spray half angles are assumed for numerical modelling, so that the LISA model can capture these variations in the spray and the atomization will be captured more accurately. However, the model is less sensitive to other parametric variations such as nozzle exit diameter (D_{inj}) and injection. Thus, to capture the better atomization of liquid sheet at higher Gas to Liquid Ratio (GLR) the use of different values of spray-half angles are considered. Also, it is seen during the nozzle testing that the spray angle expanded at the increment of the atomizing gas flow rate; hence, this assumption is reasonably acceptable.

2.1.1. Primary breakup model

The Linear Instability Sheet Atomization (LISA) built-in model from Fluent is applied to capture the primary breakup of ligaments for ETI [49,65]. The two-phase flow in the injector creates an air core surrounded by the liquid film (Fig. 2c). The thickness of this film t is related to the mass flow rate $\dot{m}_{eff}$, the nozzle exit diameter D_{inj}, the liquid density ρ_l and axial velocity of liquid film $u = U\cos\theta$ by the following relationship:

$$\dot{m}_{eff} = \pi\rho_l u t(D_{inj} - t) \tag{1}$$

The total velocity is assumed to be related to the injector pressure by:

$$U = k_v\sqrt{\frac{2\Delta P}{\rho_l}} \tag{2}$$

To ensure that the size of the air core is non-negative, the velocity coefficient k_v is given by:

$$k_v = \max\left[0.7, \frac{4\dot{m}_{eff}}{d_o^2\rho_l\cos\theta}\sqrt{\frac{\rho_l}{2\Delta P}}\right] \tag{3}$$

where spray-angle θ, and injection pressure ΔP is assumed to be known.

The model includes the effects of the surrounding gas, liquid viscosity, and surface tension on the breakup of the liquid sheet. Details of the theoretical development of the model are given in Senecal et al. [70] and are only briefly presented here. For a more robust implementation, the gas-phase velocity is neglected in calculating the relative liquid-gas velocity. This avoids having the injector parameters depend too heavily on the usually under-resolved gas-phase velocity field very near the injection location. The model assumes that a two-dimensional, viscous, incompressible liquid sheet of thickness $2h$ moves with velocity U through a quiescent, inviscid, incompressible gas medium. The liquid and the gas have densities of ρ_l and ρ_g, respectively, and liquid viscosity is μ_l. The infinitesimal wavy disturbance imposed on the initial steady motion has the form:

$$\eta = \eta_o e^{-ikx+\omega t} \tag{4}$$

where η_o is the initial wave amplitude, $k = \frac{2\pi}{\lambda}$ is the wave number, and $\omega = \omega_r + i\omega_i$ is the complex growth rate. The most unstable disturbance has the largest value of ω_r, and is assumed to be responsible for sheet breakup. The most unstable disturbance can be calculated from the dispersion relation as a function of wave number $\omega = \omega(k)$ as derived in [70].

The sheet breaks up and the ligaments formed with a length L_b as given by:

$$L_b = \frac{U}{\Omega}\ln\left(\frac{\eta_b}{\eta_o}\right) \tag{5}$$

where $\ln(\frac{\eta_b}{\eta_o})$ is an empirical sheet constant, and Ω is the maximum growth rate. Dombrowski and Hooper [71] showed that in the range of Weber numbers (We) from 2 to 200 a value of 12 for the sheet constant agreed favourably with the experimental sheet breakup lengths.

The diameter of the ligaments formed at the point of a breakup can be obtained from a mass balance. If it is assumed that the ligaments are formed from tears in the sheet twice per wavelength, the resulting diameter is given by:

$$d_L = \sqrt{\frac{8h}{K_s}} \tag{6}$$

where K_s is the wave number corresponding to the maximum growth rate Ω.

The breakup of ligaments to droplets is assumed to behave according to Weber's analysis [72]. A volume median diameter d_o is produced and is given by:

$$d_o = 1.88 d_L(1 + 3Oh)^{1/6} \tag{7}$$

Once d_o is determined, it is assumed that this droplet diameter is the most probable droplet size of a Rosin-Rammler distribution with a spread parameter of $n = 3.5$ and dispersion angle of 6°. Additional details of the model can be seen in [70].

2.1.2. Secondary breakup model

The secondary breakup of droplets to smaller ones was modelled by the Taylor Analogy Breakup (TAB) model as the Weber number is less than 100 (We<100) [20,50,64,65]. Different regimes of droplet fragmentation are determined by using the critical value of We. The hydrodynamic force required for the deformation of droplets is related to the surface tension force acting to retain the droplet form by We. Since the Ohnesorge number (Oh) remains below 0.1 (Oh≪0.1) in the computational domain, the main parameter related to breakup physics is the We [20,64,65]. The Discrete Phase Model (DPM) treated the liquid droplets in Lagrangian manner and tracked the droplets throughout their flight. The TAB and DPM models are well adapted to the conditions of spraying and validated in the earlier studies; details can be found in [20,50,51,64].

2.1.3. Droplet collision and coalescence model

In Fluent, the collision model assumes that the frequency of collisions is much less than the particle time step. This model is most applicable for low We collisions, where collision results in bouncing and coalescence. If the droplets collide head-on, then the outcome tends to be coalescence, whereas, in oblique collision, bouncing is a more likely outcome. The probability of coalescence can be related to the offset of the collector droplet centre and the trajectory of the smaller droplet. The critical offset (b_{crit}) is the distance between the centre of one drop (with radius r_2) and the relative velocity vector u_r. The relative velocity vector is supposed to be located at the centre of the second droplet (with radius r_1), see details in [73]. Here r_1 and r_2 are the radii of colliding smaller and larger droplets, respectively. Coalescence occurs when surface energy dominates, while bouncing occurs when kinetic energy dominates. The criteria, b_{crit}, determine the transition boundary between various regimes: drops coalescence when $b \le b_{crit}$, and bouncing when $b > b_{crit}$ [33,73].The critical offset is a function of the collision We_l and the relative radii of the collector and smaller droplet. O'Rourke [74] calculates the critical offset by using the expression:

$$b_{crit} = (r_1 + r_2)\sqrt{\min\left(1.0, \frac{2.4f}{We_l}\right)} \tag{8}$$

Here f is a function of $(\frac{r_1}{r_2})$ and is defined as:

$$f\left(\frac{r_1}{r_2}\right) = \left(\frac{r_1}{r_2}\right)^3 - 2.4\left(\frac{r_1}{r_2}\right)^2 + 2.7\left(\frac{r_1}{r_2}\right) \tag{9}$$

2.2. Model validation

The experiments using an effervescent atomizer nozzle by Liu et al. [32] and numerical work of Qian and Lin [43] are utilized for the validation of present numerical work. The present model and the numerical and experimental work considered here for validation use the effervescent nozzle spraying the water droplets into the atmosphere. The operating conditions of Liu et al. [32], Qian et al. [43,46] and the present numerical work are $P_{inj} = 0.6$ MPa, $D_{inj} = 0.004$ m, $m_w = 1.6$ kg/min and the GLR is varied from 0.067, 0.090, 0.132, 0.176 (as shown in Fig. 3).

Fig. 3 depicts that the present numerical model can correctly predict the value of SMD for the spray droplets along the axial direction. It is observed that the present numerical LISA model performs better for higher GLRs (0.132 and 0.176) while it shows some deviation along the axial direction from 1 to 3 cm (or 0.01–0.03 m) for lower GLRs of 0.067 and 0.090. Overall analysis shows that droplets' diameter first decreases and then increases along the axial direction [32,33,43]. This happens due to the presence of higher relative velocities between atomization gas and droplets in the near-nozzle exit region. However, in the downstream region, the droplets with lower velocities collide with each other and coalescence takes place causing an increment in the droplet diameter [43,46]. Moreover, it can be determined from these results that the increment in the GLR from 0.067 to 0.176 decreases the size of the droplets.

3. Numerical results and discussion

This section provides a detailed analysis of the effects of the group-type angular injection and effervescent-type atomization on gas dynamics and droplet dynamics inside the HVSFS torch. Also, the impact of various nanoparticles loading in liquid feedstock on the droplet breakup, evaporation and gas dynamics of the HVSFS torch will be discussed. The results are divided into different sections; firstly GTI effects on gas and droplet dynamics are examined in Section 3.1.1, and the impact of various nanoparticle concentration over droplets dynamics is covered in Section 3.1.2. Afterwards, a similar kind of analysis is developed for the ETI cases in Sections 3.2.1 and 3.2.2. Here, the Case 2.1 (STI), and Case 1 (Without Droplets) are used as reference cases for the analysis and comparison with the GTI and ETI cases.

3.1. Group-type injection (GTI)

This section illustrates the effects of varied angles of injection in the GTI on the gas and droplet dynamics inside the DJ2700 thermal spray torch. In all cases, the suspension droplets are injected with a constant diameter of 150 μm, the mean initial velocity of 42 m/s and injection mass flow rate of 1×10^{-4} kg/s, with different solid nanoparticle

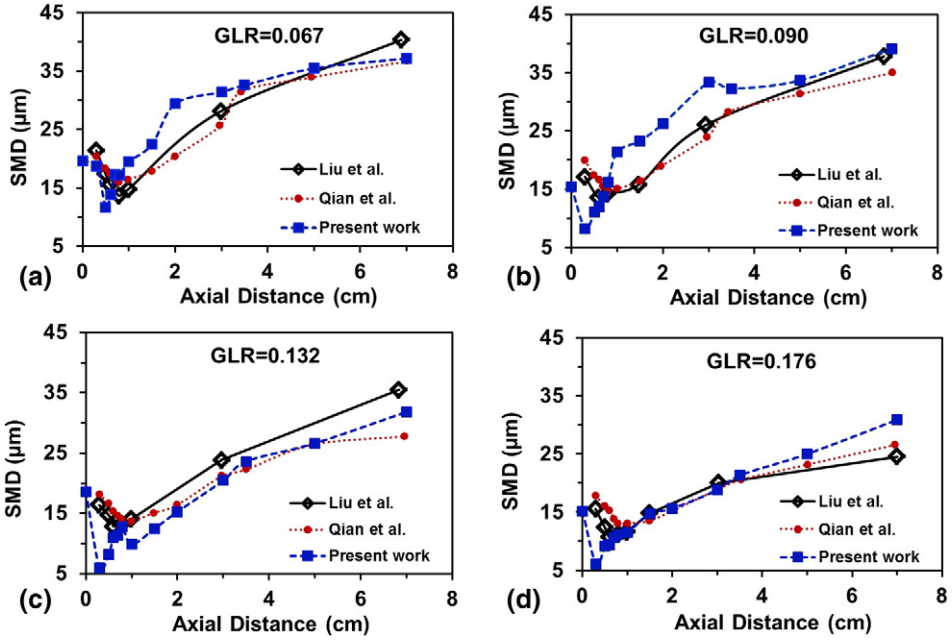

Fig. 3. Comparison of the predicted results at varied GLR with the work of Liu et al. (experimental) [32] and Qian et al. (numerical) [43,46], (a) GLR = 0.067, (b) GLR = 0.090, (c) GLR = 0.132, and (d) GLR = 0.176.

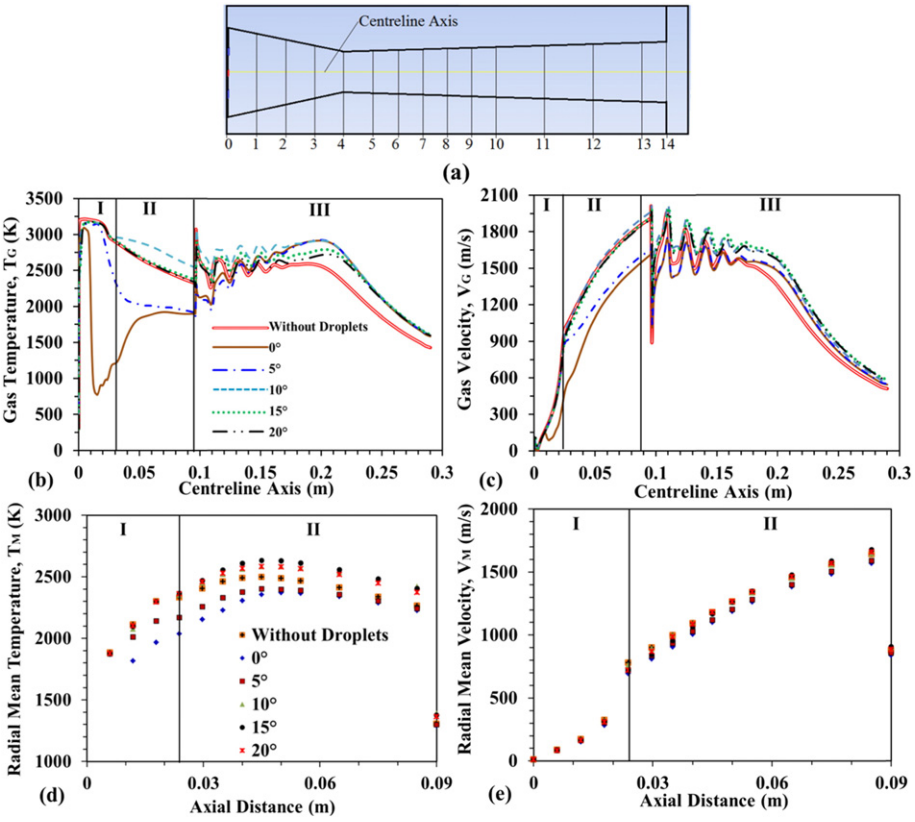

Fig. 4. (a) The torch section-I and section-II with data collection lines, (b) comparison of gas temperature, T_G, and (c) gas velocity, V_G, (d) comparison of mean radial gas temperature, T_M and (e) gas velocity, V_M, for 150 μm diameter droplet injection inside DJ2700 torch at varying angles of injections (GTI), and having 0 wt.% nanoparticle concentrations (pure-ethanol homogeneous droplets).

concentrations of 0, 5, 15, and 25 wt.%. In the GTI, the liquid feedstock is injected into the torch with different angles of injection of 5°, 10°, 15°, and 20° and named as Cases 2.2, 2.3, 2.4 and 2.5, respectively (Table 2).

3.1.1. Effects of varied angles of injection on the HVSFS gas and droplet dynamics

The flow physics in the thermal spray torch can be changed by using different types of liquid feedstock injections and varying injection parameters [50–53]. This section explains the effects on the gas flow dynamics and droplet dynamics by changing the angles of injection. In Fig. 4a, the CC section-I and the barrel section-II of the torch are shown. Gas temperature and gas velocity data are collected along the centreline axis, marked in yellow colour, and across 15 distinct transverse sections, numbered from 0 to 14 and highlighted by black lines. Fig. 4b and c demonstrates a comparison of gas temperature (T_G) and gas velocity (V_G) along the axis of the torch for the GTI with Case1 (Without Droplets) and Case 2.1 (STI). The heat is transferred from combustion gases to droplets, and then the droplets start evaporating after enough heating, which leads to the cooling of combustion gases inside the CC and in the barrel sections of the torch. It is seen in Fig. 4b that the gas cooling is reduced with the increment in the injection angle from 0° to 20°. Maximum cooling is observed for the 0° angle of injection as the pure-ethanol droplets extract heat from the hot gases and are evaporated along the torch's central axis. Whereas, minimum cooling effects are detected for 10°–20° angles of injection as the droplets are injected into the core combustion regions. Thus, less cooling effect is observed along the torch's central axis (Fig. 4b).

After the torch exit, in the free jet section-III at $x = 0.15$ m, an increase in temperature is observed for 0°–20° angles of injection as compared to Without Droplets (Case 1). This temperature rise in the free jet section-III proves the combustion of pure ethanol vapours which add heat to the combustion gases (Fig. 4b). Moreover, with an increase in the angle of injection, the droplet deviates from the centreline axis of the torch when injected into the core of the combustion zone. This technique increases the ethanol evaporation and combustion within the torch, hence improves the efficiency of the HVSFS process. From the graphical presentation in Fig. 4b and c, a 10° angle of injection appears appropriate, as it enhances the T_G and the V_G compared to all other cases. It proves that at a 10° angle of injection, ethanol droplets evaporated inside the CC, and non-premixed combustion started in the barrel section and added maximum heat and energy to the overall flow inside and outside the torch. Further, at 15° and 20° angles of injection, the T_G trend is similar to Without Droplets Case 1; hence, it is evident from these graphs that no central cooling is observed at large angles of injection.

The interaction between high energy combustion gases and droplets is also governed by the relative velocity of droplets within the continuous gas, as combustion gas has higher kinetic energy and its momentum is transferred to the droplets. Therefore, the velocity of droplets keeps increasing throughout their flight. As the flow passes through a C-D nozzle, the flow velocity, and Mach number increases, which adds the energy into the droplets and they fly from the nozzle towards the torch exit. It is seen in Fig. 4c that the V_G decreases for the 0° and 5° angles of injection along the torch axis as the droplets travel along the centreline axis. Moreover, due to cooling of the combustion gas, reduction in the temperature and the velocity of flame is detected. Whereas for higher angles of injection (10°–20°) the droplets travel far away from the centreline axis, hence the velocity drop is not detected along the torch axis. However, in the free jet section-III, an increase in T_G and V_G confirms the addition of thermal and kinetic energy from the ethanol combustion with the remnant oxygen (Fig. 4b and c).

Fig. 4d and e shows the comparison between the mean radial temperatures (T_M) and mean radial velocity (V_M) along 0–14 vertical lines shown in Fig. 4a, and it also proves that the ethanol combustion added

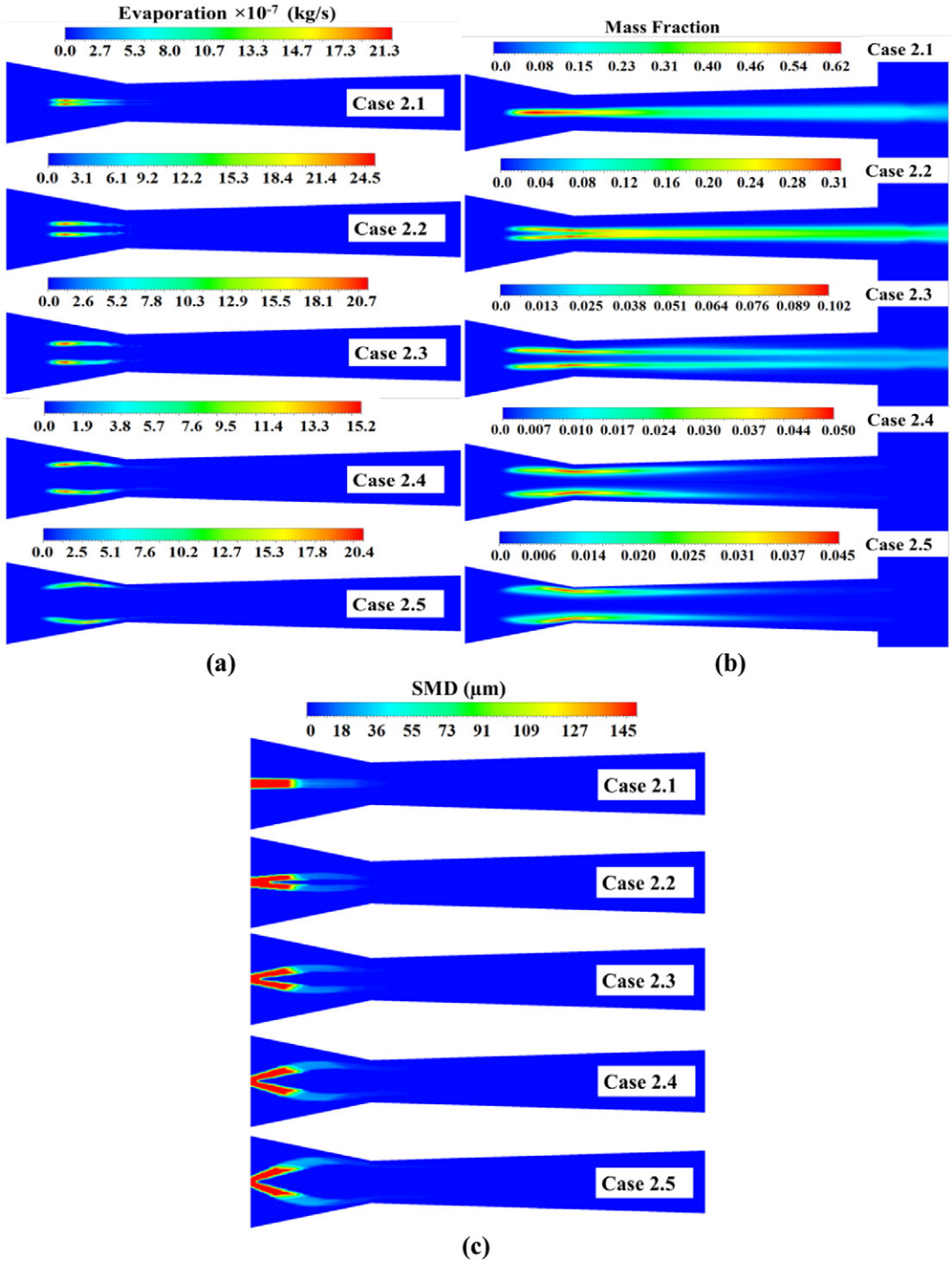

Fig. 5. Comparison of contours-map of (a) evaporation, (b) mass fraction and (c) SMD of the ethanol droplets at different angles of injections (see Table 2 for case description).

thermal and kinetic energy into the HVOF flame. In Fig. 4d, the highest values of T_M are observed for the 10°–20° angle of injections as the ethanol completely evaporates in the torch's CC and added thermal energy into the HVOF flame in the barrel section-II. However, the lowest values of T_M are observed for the 0°, and 5° angle of injection that confirms the evaporation of liquid ethanol is not completed in section-I and the gas cooling continues in the barrel section-II. Similarly, in Fig. 4e, the lower kinetic energies are observed for the lower values of angle of injection 0°–5°; whereas, higher values of V_M are observed for the bigger angle of injections (10°–20°). Therefore, it can be stated that the angular injection increases the HVSFS process efficiency by increasing droplet evaporation and vapour combustion rates while decreasing the cooling effects on the gas thermal and kinetic energies.

The interesting effects of the droplets breakup and evaporation in the CC are witnessed after the angular injection (GTI) of feedstock (Fig. 5). The ethanol droplets convert into vapours, and maximum evaporation is observed inside the CC middle region for 0°–15° angles of injection. For a 20° angle of injection, the droplets move towards the C-D nozzle throat region (Fig. 5a). As compared to 0° STI, the rate of evaporation is increased when droplets are injected at an angle of 5° and 10° GTI. A small decrease in the maximum value of evaporation is observed for 15° and 20° angles of injection (Fig. 5a) while lower mass fractions of

liquid ethanol are observed in these cases (Fig. 5b), which confirms the overall enhancement in the rate of evaporation. Moreover, the elongated evaporation regions are identified in Cases 2.4 and 2.5 as seen in Fig. 5a. This further proves that the overall evaporation of liquid droplets is augmented while the maximum value of 15.2×10^{-7} and 20.4×10^{-7} kg/s is illustrated in Cases 2.4 and 2.5, respectively (Fig. 5a). Based on these results, it is found that increasing the angle of injection intensifies the rate of evaporation of ethanol droplets inside the torch.

With the droplet evaporation, the location of the highest mass fraction of ethanol is observed around the throat region for all angles of injection (Fig. 5b). After the non-premixed combustion of ethanol droplets with the oxygen residues, the T_G increases inside and outside the torch, as shown previously in Fig. 5a. Gradually the mass fraction of ethanol decreases as the ethanol burns inside the torch. For 0°, 5° and 10° angles of injection, the ethanol cannot completely burn even after the barrel exit, and it leaves the torch without prior combustion (Fig. 5b). The reason for this delay in ethanol combustion for smaller angular injection is the incomplete evaporation of ethanol droplets within the CC and the barrel sections. While with 15° and 20° angles of injection the droplets completely burn and disappear near the barrel exit. Moreover, at larger angles of injection of 15° and 20°, the droplet mass fraction reduces abruptly which verifies the complete evaporation and consumption of ethanol for combustion. At lower angles of injection (<10°), the ethanol evaporation and combustion inside the torch are incomplete. On the other hand, at higher angles of injection (>20°), the suspension droplets can strike the CC walls. Therefore, it can be stated that to avoid the droplet impact on CC walls and to evaporate the liquid feedstock completely inside the torch, the right range for the angle of injection is from 10° to 20°.

In Fig. 5c the values of Sauter Mean Diameter (SMD) of the ethanol droplets are shown. This figure clearly shows the variation in the angle of injection and its effects on the dispersion of droplets inside the CC. In all cases, the SMD decreases gradually from the initial size of 150 μm due to droplets fragmentation inside the HVSFS torch. About 87% reduction in droplet diameter is observed from the inlet to the CC mid-section and the droplet size decrease to 20 μm. After that, in the nozzle throat region, the diameter of droplet reduces to 10 μm and then in the barrel section remains well below 10 μm. This trend is in good agreement with earlier studies in which the smaller diameter droplets evaporate easily and give out nanoparticles in the middle of the barrel section [52,53].

The results discussed above support that increasing the angle of injection from 0° to 20° injects the droplets into the mainstream of the combustion flame and hence improves the suspension droplet dispersion, heating, and evaporation. This also results in better consumption of flame kinetic energy to disintegrate the suspension droplets. The only drawback of the angular injection is the collision of suspension droplets with the CC walls. Thus, to protect the CC walls from droplets impingement while improving the overall flow physics, the angle of injection of 15° can be a good choice. As seen and analysed, at 15° angular injection the droplets do not strike the CC walls, and can breakup and evaporate completely within the core combustion region (section-I) (Fig. 5a–c). Also, this delivers extra thermal and kinetic energy to the HVSFS flame (as seen in Fig. 4b–e).

3.1.2. Effects of increasing the nanoparticle concentration on the HVSFS gas and droplet dynamics

From the above analysis (Section 3.1.1), the angle of injection of 15° is selected as the optimized angle for liquid feedstock injection, and the effect of different nanoparticle concentrations on the GTI is presented in Fig. 6. With the increment in the nanoparticle concentration from 0 wt.% to 25 wt.%, the droplet evaporation reduces (Fig. 6a). It is due to the increment in the heat required for vaporization, as the increase in the nanoparticle concentration augmented heat capacity of the droplets. Hence, the droplets absorbed more heat for vaporization and delayed the evaporation process. However, no significant variations in the SMD are observed (Fig. 6b), which proves that the increment in the suspension concentration has no effects on droplet atomization/disintegration in the HVSFS torch. Moreover, no significant effects are observed over the T_G and the V_G along the torch axis due to variation in nanoparticle concentration. These results are not presented here for brevity. However, it was concluded in the work of Gozali et al. [52] that by increasing percentage concentrations of nanoparticles in the base fluid, the rate of evaporation decreases, which causes a delay in the complete vaporization of droplets. The same is illustrated in Fig. 6a that is the suspension droplets suffer a decline in their rate of evaporation by the increment in the nanoparticles loading.

It is further explained in Fig. 7 that due to the reduction in evaporation the droplets remain unburnt inside the torch. The homogeneous ethanol droplets (0 wt.% nanoparticle concentration) disappeared in the barrel section due to complete evaporation (Fig. 7a). Moreover, for lower nanoparticles loadings (5 wt.%), the droplets vaporized completely in the barrel section and gave out the suspended nanoparticles in the barrel section (Fig. 7b). While with high concentration (15 and 25 wt.%) suspension droplets leave the gun without complete vaporization (Fig. 7c and d). This may lead to inaccuracy in the final coating and may produce porous, non-homogeneous nanostructured coating over the substrate [75,76]. The delay in evaporation of the suspension droplets causes insufficient heating of the suspended nanoparticles that may also deposit without prior melting. This can cause inclusion of unmelted particles which lead to porosity. In this way, it creates defects in the final coating which can result in serious consequences in the real applications [14,76]. Thus to avoid these discrepancies, the use of small nanoparticles loading is beneficial. However, the use of lower suspension concentrations should be balanced with the fact that the spraying of diluted suspensions is economically disadvantageous. Diluted suspensions mean lower deposition rates and longer processing times; moreover, if purchased feedstock is already in suspension form, purchasing a diluted suspension would mean buying a large amount of liquid with few “valuable” solid in it. Hence, at the industrial level, the optimization of the injection parameters are necessarily required

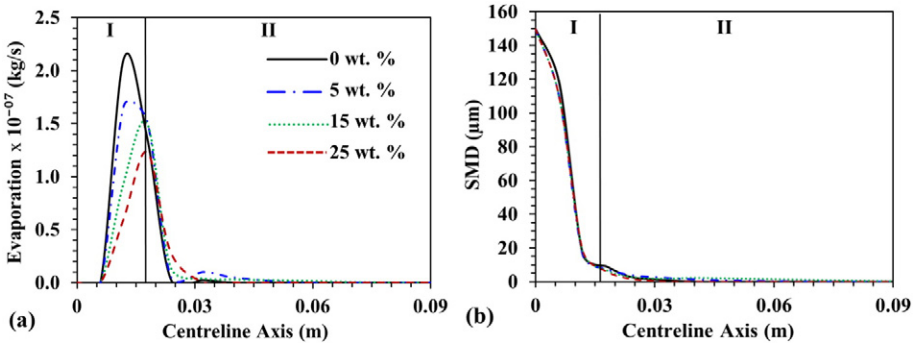

Fig. 6. Comparison of droplet (a) evaporation, and (b) SMD, with different nanoparticle concentrations of 0, 5, 15, and 25 wt.% at 15° angle of injection (GTI).

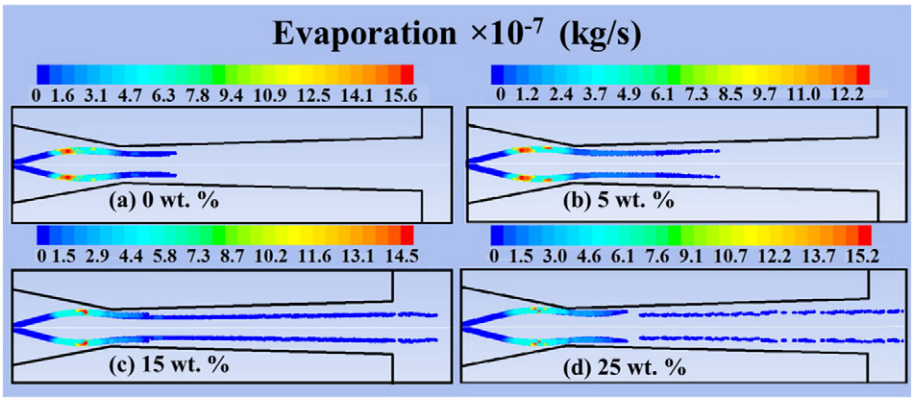

Fig. 7. Comparison of droplet evaporation with different nanoparticles concentrations of (a) 0, (b) 5, (c) 15, and (d) 25 wt.% at 15° angle of injection (GTI).

with the appropriate selection of dispersant that can also enhance the base liquid (solvent) evaporation rate to improve the nanoparticle's heating and melting processes.

3.2. Effervescent-type injection (ETI)

As stated earlier, the effervescent atomization is based on the twin-fluid flow of gas and liquid that creates a bubbly flow inside the injection nozzle and disintegrates the suspension droplets into fine mist [33,34,44]. In the ETI, the gas and liquid mixture are injected into the CC of the DJ2700 torch, and the effects of varying GLR on the gas dynamics and the droplet dynamics are investigated. The liquid injection mass flow rate remains similar as in the GTI case, i.e., 1×10^{-4} kg/s. The gas flow rates are regulated according to the selected GLR, as mentioned in Table 2. In the ETI, varied spray-half-angles of 4°, 6°, and 8° are selected based on varied GLR and named Cases 3.1, 3.2, and 3.3, respectively (Table 2).

3.2.1. Effects of varied GLR on the HVSFS gas and droplet dynamics

It is assumed that by using ETI, droplet disintegration and droplet evaporation can be augmented, and this also helps to improve the gas dynamics inside the torch. Fig. 8 illustrates the effect of variation in GLR during ETI on T_G and V_G. Compared with Case 1, ETI shows temperature reduction inside the CC and in the barrel sections due to heat absorbed by the evaporation of the droplet. The temperature difference observed between Case 1, and the smallest GLR-0.095 (Case 3.1) is $\Delta T_G = 537.31$ K in the nozzle throat region (Fig. 8a). Furthermore, the peak temperature is detected in the first shock diamond and is 200 K higher than the Without Droplets case at $x = 0.1$ m (after the nozzle exit, Fig. 8a). This is due to the heat addition by the ethanol combustion, which increases the enthalpy of the flame in the free jet region, and will help to improve the heating and melting of the suspended nanoparticles.

Moreover, comparing the results of ETI and GTI illustrates that the cooling rate is significant in the case of ETI, whereas the angular injection at 15° (GTI) shows no cooling inside the torch (Fig. 8a). This is due to the direct contact of droplets with the torch flame at a 15° angle of injection. While, in the effervescent atomization the spray-half-angles are small (4°, 6°, and 8°), and reduction in gas cooling is only possible with higher spray-half-angles. This suggests that for improving the gas flow dynamics, 15° GTI performed better than the ETI cases (Fig. 8a) and all other GTI cases (Section 3.1.1). While, in comparison to the 0° STI (Case 2.1), the ETI technique has helped to reduce the gas cooling effects, and it performs well when compared to the STI method.

For evaluating the difference between ETI and GTI further, V_G profiles are compared. They show that ETI and GTI have no significant effects on V_G as compared to Without Droplets-Case 1 in sections-I and -II (Fig. 8b). The maximum variation in T_G and V_G is observed for 0° STI that demonstrates that to minimize the losses in the thermal and kinetic energies of the HVSFS flame it is necessary to inject the suspension feedstock at an angle (using GTI) and/or using atomization nozzle (using ETI) (Fig. 8). However, the biggest positive point of using the GTI and ETI is that these injection techniques further increase the thermal and kinetic energies of the HVSFS flame in the free jet section-III and thus improve the coating process. This is because the high enthalpy flame would help to improve the heating and melting of the suspended particles which would, in turn, help in obtaining a dense coating. Moreover, a high V_G can provide high kinetic energy for accelerating the melted particulate matter and spreading the particles over the substrate to form a porosity-free coating.

Similar kinds of contour map (as presented earlier in Section 3.1.1) are developed for the ETI case to analyse the effect of varied GLR on the droplet dynamics inside the HVSFS torch. Fig. 9 shows the variation in ethanol droplets' breakup, evaporation and decreasing mass fraction due to the combustion while increasing GLR. Fig. 9a indicates the

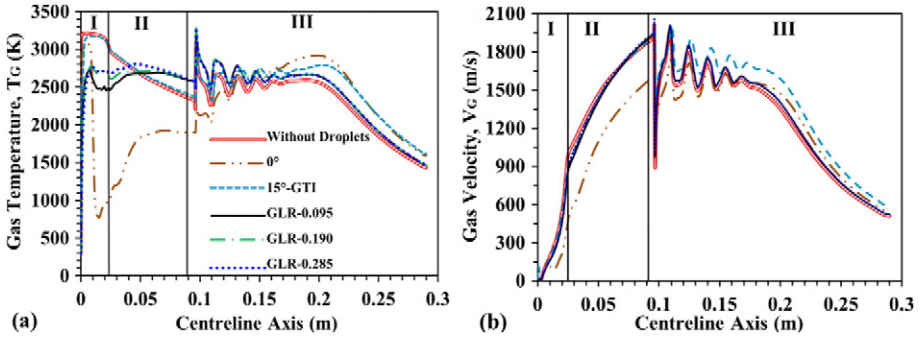

Fig. 8. Comparison of (a) gas temperature (T_G), and (b) gas velocity (V_G), for 150 μm diameter droplet injection inside DJ2700 torch at varying GLR (ETI), and having 0 wt.% nanoparticle concentrations (pure-ethanol homogeneous droplets).

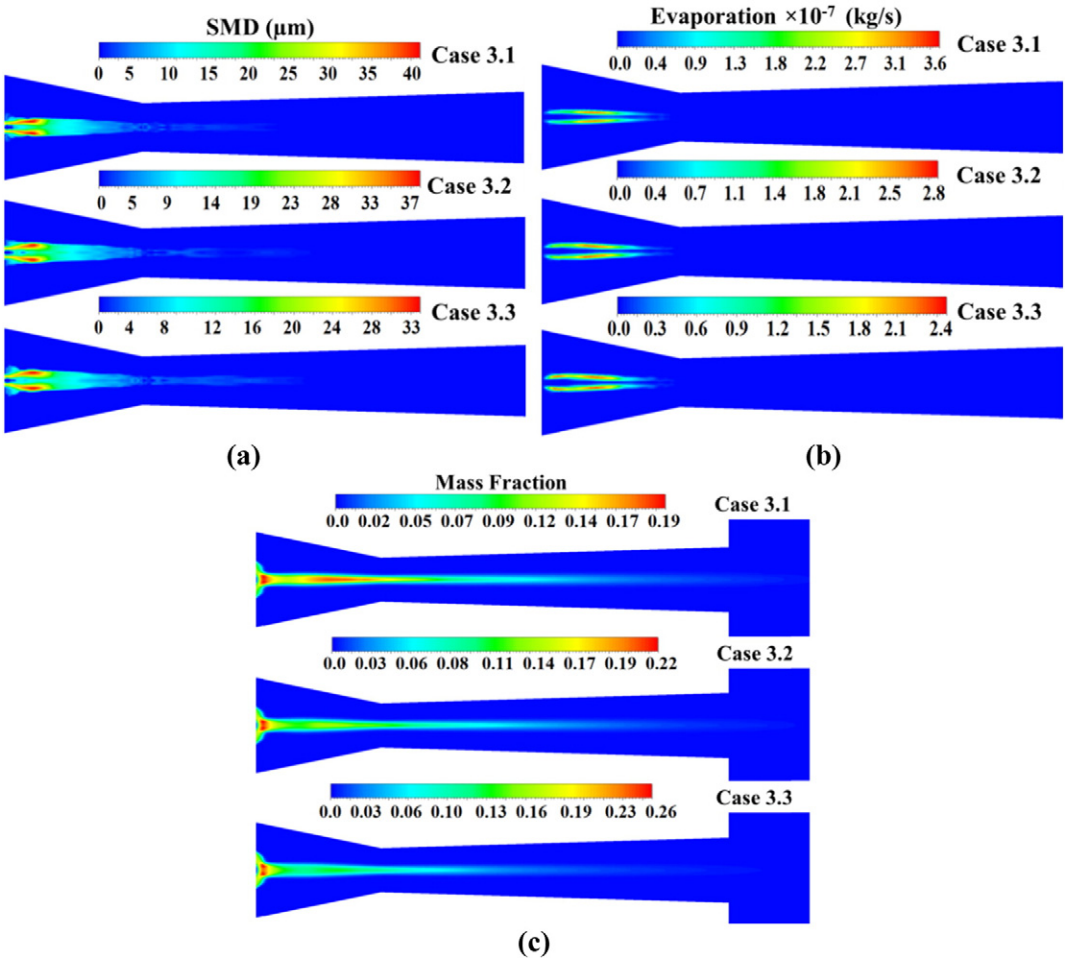

Fig. 9. Comparison of contours-map of (a) SMD, (b) evaporation and (c) mass fraction of the ethanol droplets at different GLR (see Table 2 for case description).

droplets dispersion and reduction in SMD as per increment in the GLR. The value of SMD reduces due to the increase in GLR and droplet atomization. However, the reduction is not very significant. As seen in the inlet region of the CC, droplets spread in the injection section, due to the difference in pressure between the liquid-gas mixture and high energy combustion gas, and the two-way turbulence interaction (Fig. 9a). Due to these dissimilarities, the droplet diameter reduces much faster for the ETI. The injection diameter is 150 μm and with the atomization model, it suddenly reduces to 20 μm at the point of injection, due to the gas cavity within the liquid layer. Thus, the thin liquid sheet rapidly breaks into smaller droplets due to the atomization gas effects and the highly energetic combustion gases inside the torch. It must be noted that in GTI and STI this kind of disintegration and reduction in the droplet diameter has not been observed. The benefit of the smaller suspension droplets ($d \leq 50$ μm), as analysed in an earlier study [52,53], is that they experience high evaporation in the mid-section of the nozzle

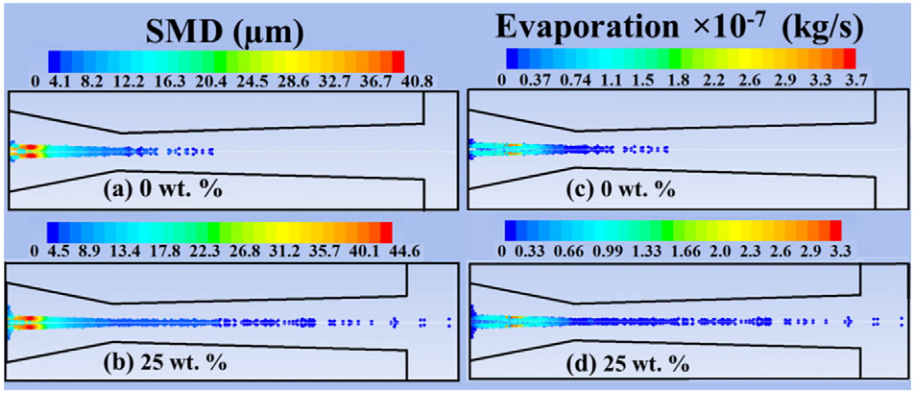

Fig. 10. Comparison of (a–b) SMD, and (c–d) evaporation of droplets with different nanoparticles concentrations of 0 and 25 wt.% for ETI at a spray-half-angle of 4° and GLR of 0.095 (Case 3.1).

and can be effectively used in applications where the suspension contains nanoparticles with a high melting point [52,53].

It can also be seen in Fig. 9a that the value of the spray-half-angle is quite small, consequently, the droplets cannot inject into the core of the combustion zone. Hence, the lower rate of evaporation is observed for the ETI when compared to the GTI (shown previously in Fig. 5a). The two red zones in Fig. 9b (for Case 3.3), demonstrate that the overall evaporation is augmented when GLR is increased. It is proved from Case 3.3 (Fig. 9c) that less ethanol is left in the barrel section, and it is completely evaporated and was burned before the torch exit. While in Cases 3.1 and 3.2, some ethanol discharges outside the torch that confirms the low rate of evaporation and combustion for lower GLR cases. Additionally, it can be said that a further increment in GLR (to increase the spray-half-angle) can augment the efficiency of the ETI. The main advantage observed for the ETI is the enormous reduction in droplet diameter that can improve the deposition properties of the HVSFS process [48].

3.2.2. Effects of increasing the nanoparticle concentration on the HVSFS gas and droplet dynamics

To analyse the effect of increasing the nanoparticles concentration over ETI, the spray-half-angle of 4° is selected with GLR of 0.095 (Case 3.1), and results are presented in this section. As discussed earlier in Section 3.1.2, increasing the nanoparticles concentration would decrease the evaporation rate for suspension droplets due to increase in the heat capacity of the liquid droplets. This is also true for the ETI, and Fig. 10 shows the different behaviour of suspension droplets for two different nanoparticles concentration of 0 wt.% and 25 wt.%. As per increment in droplet concentration from 0 to 25 wt.% the surface tension of the droplet increases, hence it reduces the droplet fragmentation inside the torch (Fig. 10a and b). A 9% reduction in the overall droplet disintegration is noticed in the SMD when the nanoparticles concentration is varied from 0 wt.% to 25 wt.%.

Moreover, the increase in nanoparticles loading (from 0 to 25 wt.%) augments the value of the heat of vaporization for the suspension, which results in lower evaporation of droplets. Fig. 10c and d compares the values of droplet evaporation for the lowest (0 wt.%) and the highest (25 wt.%) nanoparticles concentration. It is observed that the rate of evaporation decreases and the droplets leave the torch without complete evaporation for 25 wt.% nanoparticles concentration. The final locations of homogeneous and non-homogeneous droplets are significantly changed, and every 5% increment in nanoparticles concentration would change the point of complete evaporation inside the torch [52,53]. Therefore, to control the droplets disintegration and evaporation one has to control the nanoparticles concentration in the suspension. The effervescent atomization abruptly reduces the droplet size of the suspension. As the high values of GLR give smaller droplet sizes, greater evaporation can be achieved in the mid-section of the nozzle. Thus, by improving the spray-angle of the ETI technique, it can be successfully used in applications where greater concentration of suspended nanoparticles is required.

3.3. Comparison between group-type injection (GTI) and effervescent-type injection (ETI)

Most of the comparative statements are already mentioned in Section 3.2 while analysing the effects of using ETI in the HVOF torch. A further comparison between GTI and ETI droplet evaporation and droplet disintegration is shown in Fig. 11. The maximum rate of evaporation is observed for homogeneous droplets (pure-ethanol) injection at 15° angle of injection (Fig. 11a). While for ETI, even for homogeneous droplets, the rate of evaporation is significantly reduced as the droplets are not directly injected into the CC hot flame region. Moreover, as stated earlier, the rate of evaporation is reduced due to the increment in nanoparticles concentration, and this is true in both cases of GTI and ETI.

The second comparison between GTI and ETI is the droplet disintegration phenomena. As the ETI utilizes the twin-fluid criteria for droplet atomization, it works significantly better than the single-fluid injection in the GTI technique (without atomization). As seen in Fig. 11b, the initial droplet diameter reduced gradually inside the torch CC in GTI for both homogeneous and non-homogeneous suspension droplets. However, in ETI, due to the pressure difference between the atomizing gas and the suspension liquid, the droplets are shattered at the beginning of the torch CC and the reduction in the droplet diameter is significantly higher than the GTI cases (Fig. 11b). As explained in the modelling section (Section 2.1), the droplets may coalesce after the collision. In the ETI case, at the beginning of the torch's CC, the droplets firstly grow to a certain point and then start collapsing rapidly (Fig. 11b). Further, the reduction in the droplet diameter has been affected by the increment in the nanoparticles loading and as mentioned in Section 3.2.2, 9% reduction is analysed in overall droplets fragmentation. Hence, it can be said that an increase in nanoparticles concentration has small effect on droplet fragmentation inside the DJ2700 torch for ETI and GTI cases. This examination is in accordance with the analysis of Esfarjani and Dolatabadi [47].

In the original design of the DJ2700 gun, the carrier gas tube is located at the centre of the CC inlet wall and is surrounded by annular O/F inlets. Therefore, for STI and ETI injections, a recirculation zone is created close to the back wall in the injection area, and the particles start to spread out in that region. The hot combustion flame reaches the axis of the torch and interacts with the droplets. When the droplets inject at an angle of 10°–15° directed towards the combustion core they have a direct interaction with the flame which makes the evaporation process more efficient in comparison to the axial injection. For the GTI technique, one has to control the injection parameters and fixed them to avoid droplet's collision with the CC walls. After that, the droplets are evaporated and give out the nanoparticles in the barrel mid-section or after the torch exit, depending on the finishing point of the evaporation process.

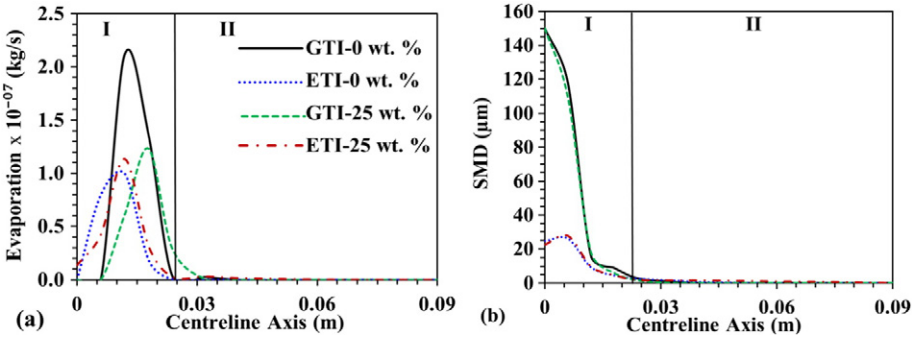

Fig. 11. Comparison of droplet (a) evaporation, and (b) SMD, with different nanoparticles concentrations of 0 and 25 wt.% at 15° angle of injection-GTI and for ETI at spray-half-angle of 4° and GLR of 0.095 (Case 3.1).

In the HVSFS process, the coating efficiency is dependent on the torch operating parameters as well as on the injection parameters. The effectiveness of the HVSFS process can be increased by modifying the design of the liquid feedstock injection system and by controlling the injection parameters. The in-flight behaviour of suspension droplets, including breakup and evaporation, has a strong link with the deposition efficiency. For sufficient heating and melting of the suspended nanoparticles, a proper injection procedure must be selected that could increase the droplet breakup and evaporation inside the torch. Also, the injection should be in such a way that it improves the ethanol combustion and heat addition to increase the efficiency of the HVSFS process. Hence, by the complete evaporation of droplets inside the CC and by sufficient heating and melting of suspended nanoparticles in the barrel section, a fine coating can be obtained. Furthermore, the atomization of precursor droplets inside the HVOF torch is a requisite for the formation of nanoparticles dense coatings, as the injection of the liquid precursor without atomization may result in large sized nanoparticles and delays the evaporation which reduces particle heating and melting that lead to the formation of the porous coating.

4. Conclusion

The increments in the nanoparticles concentrations from 0 to 25 wt.% have significant effects on the thermophysical properties of liquid feedstock. Furthermore, these properties are calculated based on the proposed nanofluids models in the literature and then used in the present modelling work. Subsequently, the effects of nanoparticles suspension on the gas dynamics and the droplet dynamics in the HVSFS process are investigated. Numerical simulations are performed for analysing the impact of angular injection and effervescent atomization. It is observed that when suspension droplets are fed into the HVSFS by using the surface-type injection (STI) at a 0° angle of injection, the gas enthalpy and kinetic energy are reduced, and the efficiency of the HVSFS flame is decreased significantly. The angular injection and effervescent atomization are selected to reduce the cooling effect and to add more energy to the HVSFS flame. The following conclusions are drawn from this work:

- The final location of the evaporation of pure ethanol and suspension droplets (homogeneous and non-homogeneous droplets) is significantly different. The increment in the nanoparticles concentration affected the properties of liquid feedstock; and viscosity, surface tension, heat capacity and thermal conductivity of the suspension droplets are increased. These variations in the thermophysical properties of the feedstock significantly affected the gas dynamics and droplet dynamics in the HVSFS torch. The highly concentrated droplet required more heat of vaporization and delayed the evaporation process of the droplets, and it leads to the cooling of the HVSFS flame, and the suspension droplets may come out of the torch without complete evaporation.
- To overcome the losses and delays in the droplet evaporation the group-type injection (GTI or continuous angular injection) can be used. It will reduce the thermal and kinetic energy losses in the HVSFS torch, and thereby improves the coating formation.
- At lower angles of injection of 5°–10°, the suspension droplets could not completely evaporate within the torch and come out without prior evaporation which can create defects in the final coating. For higher angles of injection 15°–20°, the droplets collide with the CC walls and may deposit on the torch internal wall and damage them. Hence, the angle of injection of 10°–15° is selected as the optimal value to avoid collision with the torch wall and improve the gas and droplet dynamics inside the torch.
- The effervescent-type injection (ETI) also improves the gas and droplet dynamics inside the HVSFS torch as it performs better than the STI. However, in comparison to the GTI, the effervescent atomization is not particularly effective. For further improving the atomization process of the ETI, the ratio of gas-to-liquid mass flow rate must be increased to widen the spray-half-angle. It will inject the suspension liquid into the core combustion regions and improve the droplet evaporation as noticed for the GTI. Thus, it can work more efficiently with the HVSFS process.

Abbreviations

CC	combustion chamber
C-D	convergent-divergent
CFD	Computational Fluid Dynamics
DJ	Diamond Jet
ETI	effervescent-type injection
GTI	group-type injection
HVSFS	high-velocity suspension flame spraying
HVOF	high-velocity oxygen fuel
LISA	Linear Instability Sheet Atomization
TAB	Taylor Analogy Breakup
STI	surface-type injection

Nomenclature

Symbols

d_o	volume median diameter (m)
d	droplets' diameter (μm)
d_L	diameter of ligament (m)
D_{inj}	nozzle exit diameter (m)
$2h$	liquid sheet thickness (m)
k	wave number
k_v	velocity coefficient
L_b	ligaments length (m)
$\dot{m}_{eff}$	mass flow rate (kg)
n	spread parameter
ΔP	injection pressure (MPa)
$\mathrm{Oh} = \frac{\mu}{\sqrt{\rho_d \sigma d}}$	Ohnesorge number (Oh)
t	thickness of liquid film (m)
u	Axial velocity of liquid film (m/s)
U	total velocity (m/s)
v_{rel}	relative velocity of droplets (m/s)
$\mathrm{We} = \frac{\rho_d v_{rel}^2 d}{\sigma}$	Weber number (We)

Greek symbols

μ	droplets' viscosity (kg/m·s)
ρ_d	droplets' density (kg/m^3)
ρ_c	combustion gas density (kg/m^3)
ρ_l	liquid density (kg/m^3)
ρ_g	atomization gas density (kg/m^3)
η_o	initial wave amplitude
η	infinitesimal wavy disturbance
σ	droplets' surface tension (N/m)
θ	spray angle
ω	complex growth rate
Ω	maximum growth rate

Subscripts

c	combustion gas
d	droplets

l	Liquid
rel	relative

Acknowledgements

The authors would like to acknowledge the financial support of the UK Engineering and Physical Sciences Research Council (EPSRC) project grant: EP/K027530/1. Also likes to thank the financial support of the research studentship from the NED University of Engineering and Technology, Pakistan.

References

[1] R. Gadow, A. Killinger, J. Rauch, Introduction to high-velocity suspension flame spraying (HVSFS), J. Therm. Spray Technol. 17 (2008) 655–661.
[2] A. Killinger, M. Kuhn, R. Gadow, High-Velocity Suspension Flame Spraying (HVSFS), a new approach for spraying nanoparticles with hypersonic speed, Surf. Coat. Technol. 201 (2006) 1922–1929.
[3] N. Espallargas, Future Development of Thermal Spray Coatings: Types, Designs, Manufacture and Applications, first ed. Elsevier Ltd, London, 2015.
[4] J.O. Berghaus, J.G. Legoux, C. Moreau, R. Hui, C. Decès-Petit, W. Qu, et al., Suspension HVOF spraying of reduced temperature solid oxide fuel cell electrolytes, J. Therm. Spray Technol. 17 (2008) 700–707.
[5] J.O. Berghaus, B.R. Marple, High-Velocity Oxy-Fuel (HVOF) suspension spraying of mullite coatings, J. Therm. Spray Technol. 17 (2008) 671–678.
[6] N. Stiegler, D. Bellucci, G. Bolelli, V. Cannillo, R. Gadow, A. Killinger, et al., High-velocity suspension flame sprayed (HVSFS) hydroxyapatite coatings for biomedical applications, J. Therm. Spray Technol. 21 (2012) 275–287.
[7] G. Bolelli, V. Cannillo, R. Gadow, A. Killinger, L. Lusvarghi, J. Rauch, Processing and characterisation of high-velocity suspension flame sprayed (HVSFS) bioactive glass coatings, Ceramics-Silikáty 54 (2010) 1–7.
[8] A. Killinger, R. Gadow, G. Mauer, A. Guignard, R. Vaßen, D. Stöver, et al., Review of new developments in suspension and solution precursor thermal spray processes, J. Therm. Spray Technol. 20 (2011) 677–695.
[9] J. Rauch, G. Bolelli, A. Killinger, R. Gadow, V. Cannillo, L. Lusvarghi, Advances in high-velocity suspension flame spraying (HVSFS), Surf. Coat. Technol. 203 (2009) 2131–2138.
[10] R. Gadow, A. Killinger, J. Rauch, New results in high-velocity suspension flame spraying (HVSFS), Surf. Coat. Technol. 202 (2008) 4329–4336.
[11] E. Dongmo, M. Wenzelburger, R. Gadow, Analysis and optimization of the HVOF process by combined experimental and numerical approaches, Surf. Coat. Technol. 202 (2008) 4470–4478.
[12] E. Dongmo, A. Killinger, M. Wenzelburger, R. Gadow, Numerical approach and optimization of the combustion and gas dynamics in High-Velocity Suspension Flame Spraying (HVSFS), Surf. Coat. Technol. 203 (2009) 2139–2145.
[13] E. Dongmo, R. Gadow, A. Killinger, M. Wenzelburger, Modeling of combustion as well as heat, mass, and momentum transfer during thermal spraying by HVOF and HVSFS, J. Therm. Spray Technol. 18 (2009) 896–908.
[14] G. Bolelli, J. Rauch, V. Cannillo, A. Killinger, L. Lusvarghi, R. Gadow, Microstructural and tribological investigation of high-velocity suspension flame sprayed (HVSFS) Al_2O_3 coatings, J. Therm. Spray Technol. 18 (2009) 35–49.
[15] D. Chen, E.H. Jordan, M. Gell, The solution precursor plasma spray coatings: influence of solvent type, Plasma Chem. Plasma Process. 30 (2010) 111–119.
[16] P. Fauchais, A. Joulia, S. Goutier, C. Chazelas, M. Vardelle, A. Vardelle, et al., Suspension and solution plasma spraying, J. Phys. D. Appl. Phys. 46 (2013) 224015.
[17] P. Fauchais, G. Montavon, Latest developments in suspension and liquid precursor thermal spraying, J. Therm. Spray Technol. 19 (2010) 226–239.
[18] L. Pawlowski, Suspension and solution thermal spray coatings, Surf. Coat. Technol. 203 (2009) 2807–2829.
[19] P. Fauchais, A. Vardelle, in: J. Hamid (Ed.), Thermal Sprayed Coatings Used against Corrosion and Corrosive Wear, Adv. Spray Appl., InTech 2012, pp. 3–39.
[20] R. Rampon, C. Filiatre, G. Bertrand, Suspension plasma spraying of YPSZ coatings: suspension atomization and injection, J. Therm. Spray Technol. 17 (2008) 105–114.
[21] R. Rampon, F.L. Toma, G. Bertrand, C. Coddet, Liquid plasma sprayed coatings of Yttria-Stabilized Zirconia for SOFC electrolytes, J. Therm. Spray Technol. 15 (2006) 682–688.
[22] M. Li, D. Shi, P.D. Christofides, Diamond jet hybrid HVOF thermal spray: gas-phase and particle behavior modeling and feedback control design, Ind. Eng. Chem. Res. 43 (2004) 3632–3652.
[23] H. Tabbara, S. Gu, Computational simulation of liquid-fuelled HVOF thermal spraying, Surf. Coat. Technol. 204 (2009) 676–684.
[24] S. Gu, C.N. Eastwick, K.A. Simmons, D.G. McCartney, G. McCartney, D.G. McCartney, Computational fluid dynamic modelling of gas flow characteristics in a high-velocity oxy-fuel thermal spray system, J. Therm. Spray Technol. 10 (2001) 461–469.
[25] S. Kamnis, S. Gu, T.J. Lu, C. Chen, Computational simulation of thermally sprayed WC-Co powder, Comput. Mater. Sci. 43 (2008) 1172–1182.
[26] S. Kamnis, S. Gu, N. Zeoli, Mathematical modelling of Inconel 718 particles in HVOF thermal spraying, Surf. Coat. Technol. 202 (2008) 2715–2724.
[27] N. Zeoli, S. Gu, S. Kamnis, Numerical simulation of in-flight particle oxidation during thermal spraying, Comput. Chem. Eng. 32 (2008) 1661–1668.
[28] M. Li, D. Shi, P.D. Christofides, Model-based estimation and control of particle velocity and melting in HVOF thermal spray, Chem. Eng. Sci. 59 (2004) 5647–5656.
[29] M. Li, P.D. Christofides, Computational study of particle in-flight behavior in the HVOF thermal spray process, Chem. Eng. Sci. 61 (2006) 6540–6552.
[30] M. Li, P.D. Christofides, Modeling and control of high-velocity oxygen-fuel (HVOF) thermal spray: a tutorial review, J. Therm. Spray Technol. 18 (2009) 753–768, http://dx.doi.org/10.1007/s11666-009-9309-2.
[31] M. Li, P.D. Christofides, Multi-scale modeling and analysis of an industrial HVOF thermal spray process, Chem. Eng. Sci. 60 (2005) 3649–3669.
[32] L. Liu, M. Fu, J. Wu, The distribution of SMD downstream the discharge orifices of effervescent atomizers, J. Eng. Thermophys. 22 (2001) 653–656.
[33] L. Qian, J. Lin, H. Xiong, A fitting formula for predicting droplet mean diameter for various liquid in effervescent atomization spray, J. Therm. Spray Technol. 19 (2010) 586–601.
[34] J.D. Whitlow, A.H. Lefevbre, Effervescent atomizer operation and spray characteristics, At. Sprays. 3 (1993) 137–155.
[35] R.A. Castleman, The mechanism of the atomization of liquids, Bur. Stan. J. Res. 6 (1930) 369–376.
[36] J.C. Lasheras, E. Villermaux, E.J. Hopfinger, Break-up and atomization of a round water jet by a high-speed annular air jet, J. Fluid Mech. 357 (1998) 351–379.
[37] P. Fauchais, V. Rat, C. Delbos, J.F. Coudert, T. Chartier, L. Bianchi, Understanding of suspension DC plasma spraying of finely structured coatings for SOFC, IEEE Trans. Plasma Sci. 33 (2005) 920–930.
[38] C. Li, G. Yang, Z. Wang, Formation of nanostructured TiO_2 by flame spraying with liquid feedstock, Mater. Lett. 57 (2003) 2130–2134.
[39] A. Ozturk, B.M. Cetegen, Experiments on ceramic formation from liquid precursor spray axially injected into an oxy-acetylene flame, Acta Mater. 53 (2005) 5203–5211.
[40] A.H. Lefebvre, X.F. Wang, C.A. Martin, Spray characteristics of aerated-liquid pressure atomizers, J. Propuls. Power 4 (1988) 293–298.
[41] J. Lin, L. Qian, H. Xiong, Relationship between deposition properties and operating parameters for droplet onto surface in the atomization impinging spray, Powder Technol. 191 (2009) 340–348.
[42] S.D. Sovani, P.E. Sojka, A.H. Lefebvre, Effervescent atomization, Prog. Energy Combust. Sci. 27 (2001) 483–521.
[43] L. Qian, J. Lin, Modeling on effervescent atomization: a review, Sci. China Phys. Mech. Astron. 54 (2011) 2109–2129.
[44] J. Jedelsky, M. Jicha, J. Slama, J. Otahal, Development of an effervescent atomizer for industrial burners, Energy Fuels 23 (2009) 6121–6130.
[45] M.T. Lund, P.E. Sojka, A.H. Lefebvre, P.G. Gosselin, Effervescent atomization at low mass flow rates. Part I: the influence of surface tension, At. Sprays. 3 (1993) 77–89.
[46] L. Qian, J. Lin, H. Xiong, T. Leung Chan, Theoretical investigation of the influence of liquid physical properties on effervescent atomization performance, J. Fluids Eng. 133 (2011) 101205.
[47] S.A. Esfarjani, A. Dolatabadi, A 3D simulation of two-phase flow in an effervescent atomizer for suspension plasma spray, Surf. Coat. Technol. 203 (2009) 2074–2080.
[48] H.B. Xiong, L.J. Qian, J.Z. Lin, Simulation of effervescent atomization and nanoparticle characteristics in radio frequency suspension plasma spray, J. Therm. Spray Technol. 21 (2012) 226–239.
[49] M.C. Fung, K. Inthanvong, W. Yang, J. Tu, Experimental and numerical modelling of nasal spray atomisation, Ninth Int. Conf. CFD Miner. Process Ind., Melbourne 2012, pp. 1–6.
[50] E. Gozali, S. Kamnis, S. Gu, Numerical investigation of combustion and liquid feedstock in high velocity suspension flame spraying process, Surf. Coat. Technol. 228 (2013) 176–186.
[51] E. Gozali, M. Mahrukh, S. Gu, S. Kamnis, Numerical analysis of multicomponent suspension droplets in high-velocity flame spray process, J. Therm. Spray Technol. 23 (2014) 940–949.
[52] E. Gozali, M. Mahrukh, S. Gu, S. Kamnis, Numerical investigation on effects of nanoparticles on liquid feedstock behavior in High-Velocity Oxygen Fuel (HVOF) suspension spraying, Surf. Coat. Technol. 280 (2015) 370–377.
[53] M. Mahrukh, A. Kumar, S. Gu, E. Gozali, S. Kamnis, Modelling the effects of concentration of solid nanoparticles in liquid feedstock injection on high- velocity suspension flame spray process, Ind. Eng. Chem. Res. 55 (2016) 2556–2573.
[54] M. Jadidi, S. Moghtadernejad, A. Dolatabadi, A comprehensive review on fluid dynamics and transport of suspension/liquid droplets and particles in High-Velocity Oxygen-Fuel (HVOF) thermal spray, Coatings 5 (2015) 576–645.
[55] B.E. Launder, D.B. Spalding, Lectures in Mathematical Models of Turbulence, Academic press, London, 1972.
[56] B.P. Stephen, Turbulent Flows, Cambridge university press, 2001.
[57] B.F. Magnussen, The eddy dissipation concept: a bridge between science and technology, Proc. ECCOMAS Themat. Conf. Comput. Combust., Lisbon, 2005.
[58] B.F. Magnussen, B.H. Hjertager, On mathematical models of turbulent combustion with special emphasis on soot formation and combustion, 16th Symp. Combust. Combust. Inst. 1976, pp. 719–729.
[59] M. Taleby, S. Hossainpour, Numerical investigation of high-velocity suspension flame spraying, J. Therm. Spray Technol. 21 (2012) 1163–1172.
[60] E. Gozali, S. Kamnis, S. Gu, Analysis of liquid feedstock behavior in High-Velocity Suspension Flame Spraying for the development of nanostructured coatings, Proc. Int. Therm. Spray Conf. 2013, pp. 418–423.
[61] S. Kamnis, S. Gu, 3-D modelling of kerosene-fuelled HVOF thermal spray gun, Chem. Eng. Sci. 61 (2006) 5427–5439.
[62] S. Kamnis, S. Gu, Numerical modelling of propane combustion in a high-velocity oxygen–fuel thermal spray gun, Chem. Eng. Process. Process Intensif. 45 (2006) 246–253.
[63] N. Zeoli, S. Gu, S. Kamnis, Numerical modelling of metal droplet cooling and solidification, Int. J. Heat Mass Transf. 51 (2008) 4121–4131.

[64] H. Tabbara, S. Gu, A study of liquid droplet disintegration for the development of nanostructured coatings, AICHE J. 58 (2012) 3533–3544.
[65] Ansys, Ansys Fluent Theory Guide, 2012 1–735.
[66] Y. Xuan, W. Roetzel, Conceptions for heat transfer correlation of nanofluids, Int. J. Heat Mass Transf. 43 (2000) 3701–3707.
[67] S.S. Hosseini, A. Shahrjerdi, Y. Vazifeshenas, A review of relations for physical properties of nanofluids, Aust. J. Basic Appl. Sci. 5 (2011) 417–435.
[68] B.X. Wang, L.P. Zhou, X.F. Peng, A fractal model for predicting the effective thermal conductivity of liquid with suspension of nanoparticles, Int. J. Heat Mass Transf. 46 (2003) 2665–2672.
[69] R.H. Perry, D.W. Green, Perry's Chemical Engineers' Handbook, seventh ed., 1997 published by McGraw-Hill.
[70] P.K. Senecal, D.P. Schmidt, I. Nouar, C.J. Rutland, R.D. Reitz, M.L. Corradini, Modeling high-speed viscous liquid sheet atomization, Int. J. Multiphase Flow 25 (1999) 1073–1097.
[71] N. Dombrowski, P.C. Hooper, The effect of ambient density on drop formation in sprays, Chem. Eng. Sci. 17 (1962) 291–305.
[72] C. Weber, Zum Zerfall eines Flüssigkeitsstrahles, J. Appl. Math. Mech./Zeitschrift Für Angew. Math. Und Mech. 11 (1931) 136–154.
[73] L. Qian, J. Lin, H. Xiong, Simulation of droplet-gas flow in the effervescent atomization spray with an impinging plate, Chin. J. Chem. Eng. 17 (2009) 8–19.
[74] P.J. O'Rourke, Collective Drop Effects on Vaporizing Liquid Sprays, Princeton University, 1981.
[75] E. Bemporad, G. Bolelli, V. Cannillo, D. De Felicis, R. Gadow, A. Killinger, et al., Structural characterisation of High-Velocity Suspension Flame Sprayed (HVSFS) TiO_2 coatings, Surf. Coat. Technol. 204 (2010) 3902–3910.
[76] G. Bolelli, V. Cannillo, R. Gadow, A. Killinger, L. Lusvarghi, J. Rauch, Properties of High-Velocity Suspension Flame Sprayed (HVSFS) TiO_2 coatings, Surf. Coat. Technol. 203 (2009) 1722–1732.